

# Stability and chaos of hierarchical three black hole configurations

Pablo Galaviz<sup>1,2,\*</sup>

<sup>1</sup>*School of Mathematical Science, Monash University, Melbourne, VIC 3800, Australia*

<sup>2</sup>*Theoretical Physics Institute, University of Jena, 07743 Jena, Germany*

(Dated: December 3, 2024)

We study the stability and chaos of three compact objects using post-Newtonian (PN) equations of motion derived from the Arnowitt-Deser-Misner-Hamiltonian formulation, where we include terms up to 2.5 PN order in the orbital part and the leading order in spin corrections. We perform numerical simulations of a hierarchical configuration of three compact bodies in which a binary system is perturbed by a third, lighter body initially far away from the binary. The relative importance of the different PN orders is examined. The basin boundary method and the computation of Lyapunov exponent are employed to analyze the stability and chaotic properties of the system. The 1 PN terms produce a small but noticeable change in the stability regions of the parameters considered. On the other hand, the inclusion of spin or gravitational radiation does not produce a significant change with respect to the inclusion of the 1 PN terms.

PACS numbers: 04.25.Nx, 04.70.Bw, 05.45.Pq, 05.45.Jn

## I. INTRODUCTION

The dynamics of compact objects play an important role in the evolution of galaxies and other stellar systems. Post-Newtonian (PN) techniques are a useful tool for modeling the dynamic of multiple compact objects. In astrophysical models, the gravitational radiation is included via an effective force which consider 1 PN and 2.5 PN corrections, and in some cases stellar dynamical friction. Particularly, hierarchical three black hole configurations interacting in a galactic core were recently studied by several authors. For example, intermediate-mass black holes with different mass ratios are considered in [1–3]; Simulations of dynamical evolution of triple equal-mass supermassive black holes in a galactic nuclei were performed in [4, 5]. Other astrophysical applications of multiple black hole simulations include, for example, three-body kicks [6, 7] and binary-binary encounters (see e.g. [8–12]). In the context of the final parsec problem [13, 14], three-body interactions are considered as a mechanism which can drive a binary black holes system to a separation below one parsec.

Since the 1990's there has been an increasing effort to detect and study of compact objects. The most likely source of gravitational waves are binary compact objects. Recently it was shown that the probability that more than two black holes interact in the strongly relativistic regime is, not surprisingly, very small [15]. For practical purposes, the creation of gravitational waveform templates for gravitational wave detectors is naturally focused on binary systems. Binary systems can even produce complicated waveforms when taking into account spinning black holes and eccentric orbits, e.g. [16]. On the other hand, triple systems consisting by a binary black hole and a star (e.g., a white dwarf) are

potential sources of electromagnetic counterparts associated with the mergers [17–20].

The chaotic behavior of triple systems is well known in the Newtonian case (see [21] and references therein). For binaries, it is known that chaos appears when using certain post-Newtonian approximations for systems of *spinning* binaries (see [22–28]). In the present work, we study three-body systems with PN methods, where the main technical novelty is the inclusion of the 2.5 PN terms in the orbital dynamics and up to leading order spin-orbit and spin-spin terms [29–31].

Recently, similar PN techniques were applied to the general relativistic three-body problem. Periodic solutions were studied using the 1 PN and 2 PN approximation in [32–34]. Examples of three compact bodies in a collinear configuration were considered in [35, 36], and Lagrange's equilateral triangular solution was studied including 1 PN effects in [37]. In [38], the stability of the Lagrangian points in a black hole binary system was studied in the test particle limit, where the gravitational radiation effects were modeled by a drag force. The waveform characterization of hierarchical non-spinning three-body configurations using up to 2.5 PN terms was presented in [39].

Close interaction and merger of black holes require numerical relativistic simulations. The first complete simulations using general-relativistic numerical evolutions of three black holes were presented in [40, 41]. These recent simulations show that the dynamics of three compact objects display a qualitatively different behavior than the Newtonian dynamics. In [42] the sensitivity of fully relativistic evolutions of three and four black holes to changes in the initial data was examined, where the examples for three black holes are some of the simpler cases already discussed in [40, 41]. The apparent horizon and the event horizon of multiple black holes have been studied in [43–45]. Although fully general-relativistic simulations are available, they are limited to only and small number of orbits for small separations of the black holes.

---

\* Pablo.Galaviz@monash.edu

The paper is organized as follows. In Sec. II, we summarize the equation of motion up to 2.5 post-Newtonian approximation for three spinning bodies. This is followed by a discussion of the chaos indicators that we use to characterize the triple system. In Sec. III A, we describe the numerical techniques used to solve the equation of motion, and we present some results for test cases. The perturbation of a binary system by a third object is presented in Sec. III B, where we perform numerical experiments in order to study the stability and chaos of the triple system. We conclude in Sec. IV.

### A. Notation and units

We employ the following notation:  $\vec{x} = (x_i)$  denotes a point in the three-dimensional Euclidean space  $\mathbb{R}^3$  and letters  $a, b, \dots$  are particle labels. We define  $\vec{r}_a := \vec{x} - \vec{x}_a$ ,  $r_a := |\vec{r}_a|$ ,  $\hat{n}_a := \vec{r}_a/r_a$ ; for  $a \neq b$ ,  $\vec{r}_{ab} := \vec{x}_a - \vec{x}_b$ ,  $r_{ab} := |\vec{r}_{ab}|$  and  $\hat{n}_{ab} := \vec{r}_{ab}/r_{ab}$ ; here,  $|\cdot|$  denotes the length of a vector. The mass parameter of the  $a$ -th particle is denoted by  $m_a$  with  $M = \sum_a m_a$ . Summation runs from 1 to 3. The linear momentum vector is denoted by  $\vec{p}_a$ . A dot over a symbol, like in  $\dot{\vec{x}}$ , means the total time derivative, and partial differentiation with respect to  $x^i$  is denoted by  $\partial_i$ .

In order to simplify the calculations, it is useful to define dimensionless variables (see e.g. [46]). We use as basis quantities for the Newtonian and post-Newtonian calculation the gravitational constant  $G$ , the speed of light  $c$  and the total mass of the system  $M$ . Using derived constants for time  $\tau = MG/c^3$ , length  $l = MG/c^2$ , linear momentum  $\mathcal{P} = Mc$ , spin  $\mathcal{S} = M^2G/c$  and energy  $\mathcal{E} = Mc^2$ , we construct dimensionless variables. The physical variables are related with the dimensionless variables by means of a scaling, for example denoting with capital letters the physical variables with the usual dimensions and with lowercase the dimensionless variable we define for a particle  $a$  its position  $\vec{x}_a := \vec{X}_a/l$ , linear momentum  $\vec{p}_a := \vec{P}_a/\mathcal{P}$  and mass  $m_a = M_a/M$  (notice that  $m_a < 1, \forall a$ ).

## II. EVOLUTION METHOD

### A. Equations of motion

In the ADM post-Newtonian approach, it is possible to split the orbital and spin contribution to the Hamiltonian (see e.g. [47, 48])

$$H(\vec{x}_a, \vec{p}_a, \vec{s}_a) = H(\vec{x}_a, \vec{p}_a)_{\text{Orb}} + H(\vec{x}_a, \vec{p}_a, \vec{s}_a)_{\text{Spin}}, \quad (1)$$

where each component forms a series with coefficients which are inverse powers of the speed of light. We included terms up to 2.5 PN contributions where the orbital part for three bodies is given by [34, 39, 49]

$$H_{\text{Orb}} = H_{\text{N}}^{(0)} + H_{\text{PN}}^{(1)} + H_{\text{PN}}^{(2)} + H_{\text{PN}}^{(2.5)}. \quad (2)$$

Here each term of the Hamiltonian is labeled by a superscript  $n$  which denotes the PN order (powers of  $c^{-2n}$ ) and a subscript which distinguishes between the Newtonian contribution and the PN components. The spin contribution forms a power series which up to leading order is given by [50–53] (see also [31] where the next-to-leading terms are presented)

$$H_{\text{Spin}} = H_{\text{SO}}^{\text{LO}} + H_{\text{SS}}^{\text{LO}} + H_{\text{S}^2}^{\text{LO}}. \quad (3)$$

In this case, the superscript labels the leading order terms (LO) and the subscript distinguishes between the kind of interaction: spin-orbit (SO), spin(a)-spin(b) (SS) or spin(a)-spin(a) ( $\text{S}^2$ ). We specify the initial spin of the particles by using a dimensionless parameter  $\chi_a \in [0, 1]$  and the two spherical angles  $\theta_a$  and  $\phi_a$ . The initial spin of the particles is given by

$$\vec{s}_a(0) = \chi_a m_a^2 (\cos \phi_a \sin \theta_a \hat{x} + \sin \phi_a \sin \theta_a \hat{y} + \cos \theta_a \hat{z}), \quad (4)$$

where  $\hat{x}$ ,  $\hat{y}$  and  $\hat{z}$  are the unitary basis vectors in Cartesian coordinates. Using the Hamiltonian (1), the equations of motion are

$$\dot{x}_a^i = \frac{\partial H}{\partial p_a^i}, \quad (5)$$

$$-\dot{p}_a^i = \frac{\partial H}{\partial x_a^i}, \quad (6)$$

$$\dot{s}_a^i = \frac{\partial H}{\partial s_a^j} s_a^k \epsilon_{ijk}. \quad (7)$$

The first term in (2) is the Hamiltonian for  $n$ -particles interacting under Newtonian gravity

$$H_N^{(0)} = \frac{1}{2} \sum_a^n \frac{\vec{p}_a^2}{m_a} - \frac{1}{2} \sum_{a,b \neq a}^n \frac{m_a m_b}{r_{ab}}. \quad (8)$$

The explicit form of the PN terms of (2) and the equation of motion for three compact objects can be found in [39] (see also [34, 49]). The terms of the spinning part (3) for  $n$  compact objects are given in [31].

### B. Chaos indicators

There are a number of methods for diagnosing chaos in a dynamical system. For example, the Poincaré surface (for system with less than 3 degrees of freedom), the Kolmogorov-Sinai entropy, characteristic Lyapunov exponent and the fractal basin boundary method among others (see e.g. [54–56]). For our analysis, we employ the fractal basin boundary method and Lyapunov exponent. In this section, we describe the implementation of both methods.

The basin boundary method and the Lyapunov exponents are able to characterize a different type of chaos. The basin boundaries shows if a dynamical system has sensitive dependence on initial conditions which results in a different final state. However, it does not distinguish

the differences for orbits of the same type. On the other hand, the Lyapunov indicator characterize the regularity or chaos of the orbits in a way which is independent of the asymptotic behavior.

### 1. Fractal basin boundary

A dynamical system usually exhibits a transient behavior followed by an asymptotic regime. The time-asymptotic behavior defines attracting sets in the phase-space which are called attractors. The attractor can be periodic, quasi-periodic or chaotic. The closure of the set of initial conditions which has a particular attractor is called its basin of attraction. Basin boundaries for a typical dynamical systems can be either smooth or fractal [56, 57]. A system with fractal basin boundaries is sensitive to an initial uncertainty. Given  $\epsilon > 0$ , we call an initial condition point  $P^*$  unsafe if there is another initial condition point  $P$  inside a neighborhood of size  $\epsilon$  centered at  $P^*$  which converges to a different attractor. The fraction  $f$  of unsafe points is related to  $\epsilon$  by

$$f(\epsilon) \sim \epsilon^{D-d_f}, \quad (9)$$

where  $D$  is the dimension of the phase space and  $d_f$  is the dimension of the basin boundary (see [56, 58] for a detailed discussion). It is useful to define a *uncertainty exponent*  $\alpha = D - d_f$ , which satisfy the relation  $0 < \alpha \leq 1$ . The value of  $\alpha$  quantifies the presence of chaos in a basin boundary,  $\alpha \approx 1$  for regular boundaries and  $\alpha \approx 0$  for a chaotic region.

There are many ways of measure the dimension of a fractal [57, 59]. We employed the *box dimension* which is defined by

$$d_{\text{box}} := \lim_{\delta \rightarrow 0} \frac{\ln(N_\delta(A))}{\ln(1/\delta)}, \quad (10)$$

where  $A$  is a nonempty bounded set in  $d_E$ -dimensional Euclidean space and  $N_\delta(A)$  is the smallest number of sets in a  $\delta$ -cover of  $A$  (a  $\delta$ -cover of  $A$  is a collection of sets of diameter  $\delta$  whose union contains  $A$ ). For a physical or numerical experiment, there is a narrow resolution of a fractal basin boundary. The fractal is represented by an image formed by pixels of size  $l_{\text{res}}$ . In order to estimate the dimension of the basin boundary, we compute the quotient  $\ln(N_{\delta_n}(A))/\ln(1/\delta_n)$  for a set of  $\delta_n \geq l_{\text{res}}$ . The typical behavior of the resulting data is well approximated by a straight line. A linear regression method is used to fit a linear function to the resulting data (where  $\delta_n = n l_{\text{res}}$  and  $n \in \{1, 2, \dots, 12\}$ ). Therefore, the value of the intersection with the  $Y$ -axis gives an estimate value of the dimension. We tested the method by computing the dimension of non-fractal one-dimensional sets (i.e., a regular basin boundary) and Sierpinski's gasket and carpet.

### 2. Lyapunov exponent

Lyapunov exponents give another means of characterizing chaos in a dynamical system (see e.g. [54]). For an autonomous  $n$ -dimensional system

$$\dot{\vec{X}} = \vec{F}(\vec{X}), \quad (11)$$

a given reference solution  $\vec{X}_*$  and a nearby solution  $\vec{X} = \vec{X}_* + \delta\vec{X}$ , the evolution of the difference  $\delta\vec{X}$  is given by the linearized equation

$$\delta\dot{\vec{X}} = \mathbf{J}(\vec{X}_*) \cdot \delta\vec{X}, \quad (12)$$

where  $\mathbf{J}(\vec{X}_*)_{i,j} := \partial_j F_i(\vec{X}_*)$  is the Jacobian matrix of  $\vec{F}$  evaluated at the reference solution  $\vec{X}_*$ . The solution of (12) is given by [60]

$$\delta\vec{X}(t) = e^{\mathbf{J}t} \cdot \delta\vec{X}(0). \quad (13)$$

The Lyapunov exponents are defined in terms of the eigenvalues  $\Lambda_i(t)$  of the distortion matrix  $\mathbf{\Lambda} := e^{(\mathbf{J}+\mathbf{J}^T)t}$

$$\lambda_i := \lim_{t \rightarrow \infty} \frac{1}{2t} \ln \Lambda_i(t). \quad (14)$$

Sensitive dependence on initial conditions corresponds to  $\lambda_i > 0$ . Therefore, in order to distinguish between regular and chaotic orbits, it is sufficient compute the principal Lyapunov exponent  $\lambda_p := \max(\lambda_i)$ . Calculating  $\lambda_p$  directly is expensive from the computational point of view. However, using the evolution of the difference  $\delta\vec{X}$  it is possible to obtain an estimation of  $\lambda_p$

$$\lambda_p^* := \lim_{t \rightarrow \infty} \lim_{\delta X(0) \rightarrow 0} \frac{1}{t} \ln \left( \frac{\delta X(t)}{\delta X(0)} \right), \quad (15)$$

where  $\delta X(t) = |\delta\vec{X}|$ . The norm  $|\delta\vec{X}|$  plays an important role in the computation of the Lyapunov indicator (we will refer as Lyapunov indicator to  $\lambda_p^*$  in order to distinguish it from the principal Lyapunov exponent). Particularly, in the case of general relativity, additional gauge effects can affect the estimation of the Lyapunov indicator [23, 55, 61]. The results given in the literature are applied to general relativistic dynamic of test particles or to binary system in the center of mass frame. Additionally, the estimation of  $\lambda_p$  is often computed using the two-particle method instead of the evolution of the difference (see e.g. [62]). Therefore, the computation of Lyapunov indicator is new in the context of three compact objects. In order to determine gauge effects we computed  $\lambda_p^*$  (or an equivalent expression) using 4 norms: the Cartesian length of the difference vector  $\delta\vec{X}$ , the sum of the Cartesian length of the three spatial difference vectors  $\sum_a |\delta\vec{x}_a|$ , the Cartesian and proper length of  $\delta\vec{x}_3$ . In the last case an additional equation should be solved to obtain the proper time [55] using the 2 PN metric given in [63, 64]. Our results shows a small difference at the

beginning of the evolution and a negligible difference at the end. We present the results in terms of the Cartesian length of  $\delta\vec{X}$ .

Notice that in practice the Lyapunov indicator is computed approximating the limits using a *sufficient small*  $\delta\vec{X}(0)$  and *sufficient large* integration time. In our simulations, we used  $|\delta\vec{X}(0)| = 10^{-9}$ . The integration time depends on the system (see Sec. III). The evolution is performed by solving numerically the system of equations (5)-(7), therefore  $\vec{X} = (\vec{x}_a, \vec{p}_a, \vec{s}_a)^T$  is a vector with 27 components. The right hand side of (11) is the vector

$$\vec{F} = \left( \frac{\partial H}{\partial p_a^i}, -\frac{\partial H}{\partial x_a^i}, \frac{\partial H}{\partial s_a^j} s_a^k \epsilon_{ijk} \right), \quad (16)$$

and the equation of motion for the difference  $\delta\vec{X} = (\delta\vec{x}_a, \delta\vec{p}_a, \delta\vec{s}_a)$  is

$$\delta\dot{x}_a^i = \delta\vec{X} \cdot \nabla \frac{\partial H}{\partial p_a^i}, \quad (17)$$

$$-\delta\dot{p}_a^i = \delta\vec{X} \cdot \nabla \frac{\partial H}{\partial x_a^i}, \quad (18)$$

$$\delta\dot{s}_a^i = \delta\vec{X} \cdot \nabla \frac{\partial H}{\partial s_a^j} s_a^k \epsilon_{ijk}, \quad (19)$$

where we define the auxiliary operator

$$\delta\vec{X} \cdot \nabla := \sum_{b=1}^3 \sum_{j=1}^3 \left( \delta x_b^j \frac{\partial}{\partial x_b^j} + \delta p_b^j \frac{\partial}{\partial p_b^j} + \delta s_b^j \frac{\partial}{\partial s_b^j} \right). \quad (20)$$

### III. SIMULATIONS AND RESULTS

#### A. Numerical method

We solve the equations of motion numerically using the GNU Scientific Library (GSL) [65] and the OLLIPTIC code infrastructure [42]. We generate the right hand side (RHS) of the equations of motion (5)-(7) with MATHEMATICA 7.0 [66].

The simulations were done using the embedded Runge-Kutta Prince-Dormand (8,9) method provided by the GSL. We use an scaled adaptive step-size control (see [65] for details). In our simulations, the error control for the dynamical variables  $(\vec{x}_a, \vec{p}_a, \vec{s}_a)$  was set to  $10^{-11}$  and  $10^{-6}$  for the variation variables  $(\delta\vec{x}_a, \delta\vec{p}_a, \delta\vec{s}_a)$ . We use as indicator of the accuracy the estimate of the local error provided by the GSL routines and the conservation of the Hamiltonian for the simulations which do not included the radiation term.

For our stability analysis, we solve the system of equations (5)-(7) and (17)-(19) simultaneously. In order to perform the simulations in an efficient way, we adapted the number of variables depending on the problem. The parameters to consider are the number of bodies  $nb$ , the magnitude of the spin  $\vec{s}_a$  and whether we solve a planar or non-planar problem. As we mention before, the RHS

of Eqs. (5)-(7) is generated by a MATHEMATICA script. However, the RHS of Eqs. (17)-(19) becomes too large after the inclusion of 2 PN corrections. A typical computational source file for the RHS which includes 2 PN corrections has a size of 25 megabytes. The inclusion of spin produces files with a size of a hundred megabytes. Therefore, when the compilation or optimization becomes an issue, instead of computing the RHS of Eqs. (17)-(19) with the MATHEMATICA script we compute it numerically. The system (17)-(19) is the Jacobian matrix of (16). The problem reduces to the computation of

$$J_{i,j} = \frac{\partial F_i(\vec{X}_*)}{\partial X^j}. \quad (21)$$

A simple finite difference method of 2nd, 4th or even 6th order with a fix step size  $h$  does not produce an accurate solution. The main issue is the nature of the components, for example the position variables require a different optimal step-size than the momentum or the spin variables. We implemented an adaptive method based on the GSL differentiation routine. The method produces solution with an estimated error below  $10^{-8}$  (see Sec. III A 1).

An important issue in the numerical integration of a three-body system arises when two of the bodies are very close each other. In the case of adaptive step size methods, it is necessary to reduce the step size in order to resolve properly the orbits in the close interaction. An usual approach to cure this problem is to perform a regularisation of the equations of motion, see e.g., [67–71] and references therein. However, in our simulations we include a different criteria. We monitor the absolute value of each conservative part of the Hamiltonian (1) relative to the sum of the absolute values

$$H_i^{\%} := 100 \left( \frac{|H_i|}{|H_N^{(0)}| + |H_{PN}^{(1)}| + |H_{PN}^{(2)}| + L_1(H_{\text{Spin}})} \right). \quad (22)$$

A simulation stop when the contribution of the first post-Newtonian correction is larger than 10%. Empirical results show that in a similar configuration the resulted waveform shows the characteristic growth of the merger phase [39]. Therefore, the dynamics which follows after our stopping criteria may lead to the merger of two of the bodies. We will refer to the stopping criteria  $H_1^{\%} > 10\%$  as strong interaction. In order to determine safely whether there is a merger or not, it is necessary to employ a different technique able to follow the merger accurately.

We consider additionally the Newtonian escape energy of each body with respect to the other two components

$$E_{\text{esc}}^a := \frac{1}{2} \mu_a \left( \frac{\vec{p}_a}{m_a} - \frac{\vec{p}_a^*}{m_a^*} \right)^2 - \frac{\mu_a}{|\vec{x}_a - \vec{x}_a^*|}, \quad (23)$$

where  $\mu_a := m_a m_a^*$ ,  $m_a^* := \sum_{b \neq a} m_b$ ,  $\vec{x}_a^* := (m_a^*)^{-1} \sum_{b \neq a} m_b \vec{x}_b$  and  $\vec{p}_a^* := \sum_{b \neq a} \vec{p}_b$ . The simulation stops when  $E_{\text{esc}}^a > 0$  for one of the bodies and the size of the system  $S := \sum_a |\vec{x}_a|$  is 100 times the initial size

(during a strong interaction of two of the bodies it is common to have for a short time a positive value of  $E_{\text{esc}}^a$ , the second condition exclude that cases). We perform several tests to estimate the numerical errors. Here we summarize the results of these tests.

### 1. Numerical tests

Our first test was done with Lagrange's triangle solution for the Newtonian case with an initial separation  $r_{12} = r_{23} = r_{31} = 100$ , mass ratio 1:10:100 and zero eccentricity. This configuration is unstable and after 14 orbits one of the bodies is ejected from the system. The unstable property is reflected in the Lyapunov indicator  $\lambda_p^*$ . Fig. 1 (a) shows  $\log_{10}(\lambda_p^*)$  computed using two methods for the prescription of the RHS of Eqs. (17)-(19). The first method is the analytic expression (labeled  $J_a$ ) and the second the numerical solution (labeled  $J_n$ ). The two methods produces solutions which are not distinguishable in the plot (the maximum relative difference is  $4 \times 10^{-6}$ ). The Lyapunov indicator exhibits the characteristic behavior of a chaotic system. After  $t = 10^4$ ,  $\lambda_p^*(t)$  oscillates around a constant value. Fig. 1 (b) shows the relative variation of the Hamiltonian

$$\Delta H := \frac{H(0) - H(t)}{H(0)}, \quad (24)$$

for the same solution. The conservation of the Hamiltonian shows a similar behavior using the analytical expression or the numerical solution of the Jacobian. The Hamiltonian exhibits a variation of around  $10^{-12}$  before the evolution stops.

Fig. 1 (c) shows the  $L_2$  norm of the estimated errors for Lagrange's triangle solution. By looking at the errors, it is clear the difference between the solution produced using  $J_n$  and the one using  $J_a$ . The numerical solution generates errors which are two orders of magnitude larger than the analytical solution. However, even using the numerical Jacobian the accuracy is good, keeping the errors below  $1.5 \times 10^{-8}$ .

A second test was done for an stable system. Using the 1 PN equations of motion, we computed the Lyapunov indicator  $\lambda_p^*$ , the relative variation of the Hamiltonian  $\Delta H$  and the  $L_2$  norm of the estimated errors for the Hénon's criss-cross solution [32, 72, 73] (in this test we are not including post-Newtonian corrections to the initial parameters). As in the previous case,  $\lambda_p^*$  does not shows a significant difference when is computed using  $J_a$  or  $J_n$  (see Fig. 2). In this case  $\lambda_p^*$  decreases monotonically almost like a straight line; this is the characteristic behavior of a regular solution. The maximum relative difference in  $\lambda_p^*$  using  $J_a$  and  $J_n$  is  $8 \times 10^{-6}$ . The Hamiltonian is conserved with a maximum variation of  $5 \times 10^{-11}$ . The  $L_2$  norm of the estimated errors shows again a bigger noisy errors using  $J_n$  respect to the result using  $J_a$ .

A third test was done with a known chaotic binary system. We use a chaotic eccentric configuration with

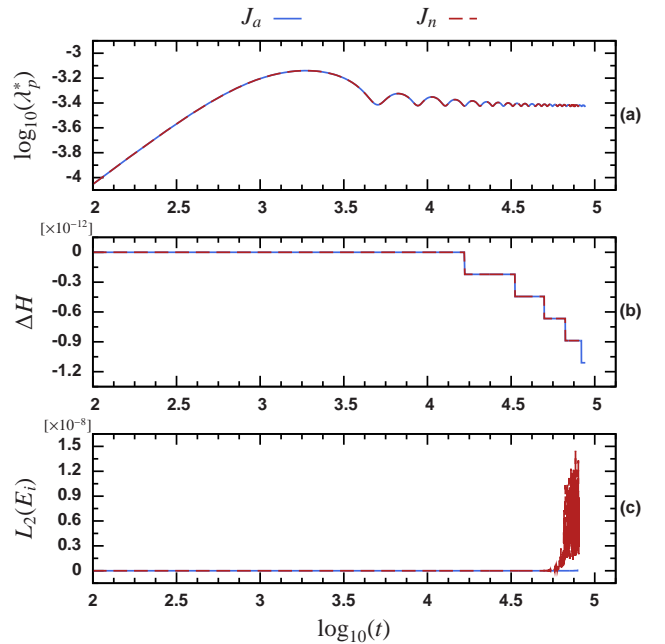


FIG. 1. Newtonian Lagrange's triangle solution. The upper panel (a) shows the Lyapunov indicator  $\lambda_p^*$ , the middle panel (b) shows the conservation of the Hamiltonian  $\Delta H$  and the lower panel (c) shows the  $L_2$  norm of the estimated errors. In every panel, the solid line denotes the solution obtained using the analytical Jacobian and the dashed line the result provided by the numerical computation of the Jacobian.

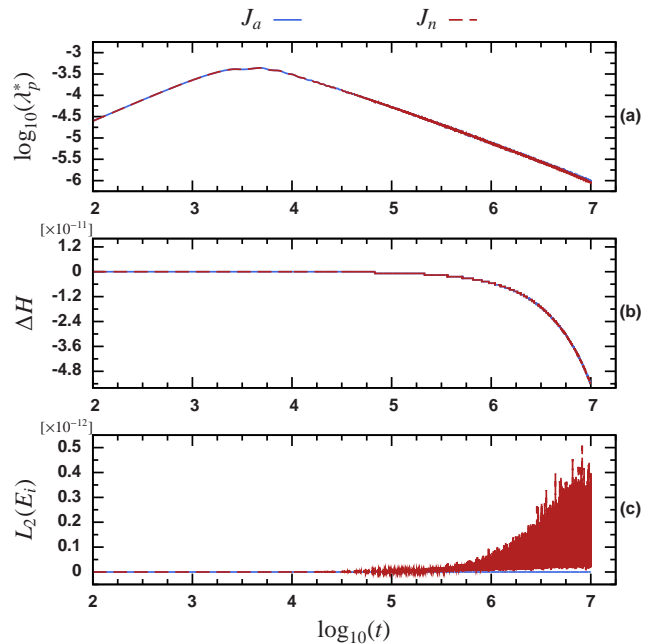


FIG. 2. 1 PN Hénon Criss-cross solution. The upper panel (a) shows the Lyapunov indicator  $\lambda_p^*$ , the middle panel (b) shows the conservation of the Hamiltonian  $\Delta H$  and the lower panel (c) shows the  $L_2$  norm of the estimated errors. In every panel, the solid line denotes the solution obtained using the analytical Jacobian and the dashed line the result provided by the numerical computation of the Jacobian.

mass ratio 3:2 and initial parameters:

$$\begin{aligned}
\vec{r}_{12}(0) &= 50\hat{x} \\
\vec{p}_1(0) &= -\vec{p}_2(0) = 0.0061644\hat{y} + 0.003616\hat{z}, \\
\vec{s}_1(0) &= -0.43765200\hat{x} - 0.11469240\hat{y} + 0.29478960\hat{z}, \\
\vec{s}_2(0) &= -0.02443680\hat{x} + 0.10324000\hat{y} - 0.01104320\hat{z}.
\end{aligned}
\tag{25}$$

A similar system, with a different units convention, was studied in [74] (Sec. IV-C1). Following [74], we solved the equation of motion using up to 2 PN correction for the orbital part and leading order in the spin. As was emphasized in [74], in this configuration the two compact bodies are rather close to each other. In order to obtain an accurate physical description, it is necessary to include higher PN corrections. The 1 PN contribution to the Hamiltonian (22) during a close encounter of the bodies can reach 50%. At this point it is important to recall one of the conclusions of [74]. Using up to 2 PN Hamiltonian with leading order spin contributions, there is not evidence of chaotic systems for configurations which are physically valid to the PN order considered. Therefore, for this test we switched off the stop condition  $H_1^{\%} > 10\%$ .

The result for the third test is presented in Fig. 3. The system was evolved using the parameters given in (25), and for reference, a non-chaotic orbit with the same initial condition but with  $\vec{s}_1(0) = \vec{0}$ . Fig. 3 (a) shows the Lyapunov indicator for the chaotic configuration (solid line) and the arithmetic mean computed for  $t > 10^6$ . The estimated value of the Lyapunov indicator is  $\langle \lambda_p^* \rangle = 10^{-5}$  (dotted line) with a standard deviation of  $1.3 \times 10^{-6}$  which correspond to a relative variation of 13%. In contrast, the regular solution shows that  $\lambda_p^*$  decreases almost monotonically after  $t = 10^4$ . In both simulations, the Hamiltonian is numerical conserved below  $10^{-8}$  (see Fig. 3 (b)), and the estimated errors are of order  $10^{-6}$  for the chaotic solution and  $10^{-10}$  for the regular solution. The main contribution to the errors in the case of the chaotic solution is due to the numerical calculation of the Jacobian matrix.

We perform additional tests already presented in Sec. III-A of [39]. A direct comparison with the results in [39] does not show significant differences in the results. For brevity, we do not display the results of the tests.

## B. Stability of hierarchical systems

Here, we consider the strong perturbation of a binary compact object system due to a third smaller compact object. As a basic configuration we study a Jacobian system with mass ratio 10:20:1. The inner binary system has initial *apo-apsis* (i.e. maximum separation of a Keplerian orbit)  $r_b(0) = 130$  and eccentricity  $e_b(0) = 0$ . Although, there are methods in post-Newtonian dynamics to specify initial parameters of a binary system with a given eccentricity (see e.g. [74–79]), in the case we are considering here, the inner binary is strong-perturbed by a third body. Therefore, it is necessary to consider addi-

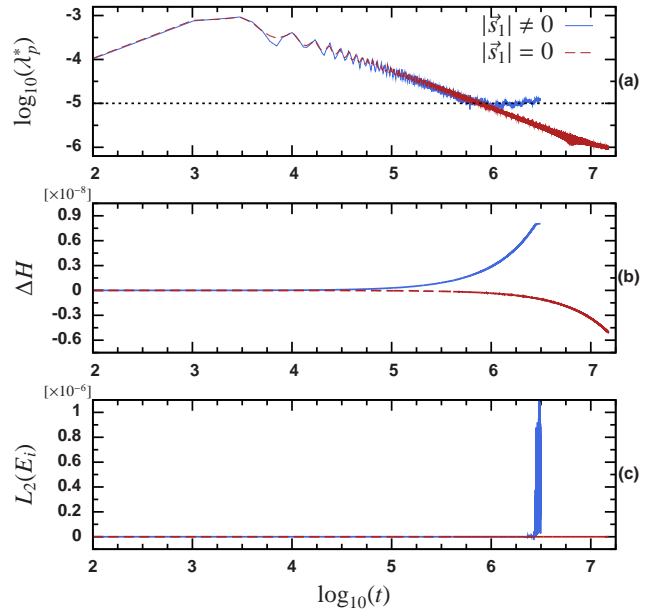


FIG. 3. Spinning binaries with an eccentric orbit. Lyapunov indicator  $\lambda_p^*$  (a), conservation of the Hamiltonian  $\Delta H$  (b) and the  $L_2$  norm of the estimated errors, for the system with initial parameters given by (25) (solid line) and the same configuration except for  $\vec{s}_1(0) = \vec{0}$  (dashed line).

tional effects. For simplicity, we set the initial parameters considering only the Newtonian dynamics of a non-perturbed binary. In particular, the eccentricity refers to the Newtonian case. In this approach, we view the third compact body and the center of mass of the inner binary as a new binary (we will refer to it as the external binary). The bodies start from a configuration where the initial radial vector  $\vec{r}_{12}$  is perpendicular to initial vector position  $\vec{x}_3$  of the external body (see Fig. 4). We denote the inclination angle between the osculating orbital planes  $\Pi_{\text{in}}$  and  $\Pi_{\text{ext}}$  by  $\iota$  (see Fig. 4). To be more specific, the initial position and momentum of each body is given by

$$\begin{aligned}
\vec{x}_1 &= \frac{m_2}{m_b} r_b \hat{x} - m_3 r_3 (\hat{y} \cos i + \hat{z} \sin i), \\
\vec{x}_2 &= \frac{m_1}{m_b} r_b \hat{x} - m_3 r_3 (\hat{y} \cos i + \hat{z} \sin i), \\
\vec{x}_3 &= m_b r_3 (\hat{y} \cos i + \hat{z} \sin i), \\
\vec{p}_1 &= -p_b \hat{y} - \frac{m_1}{m_b} p_3 \hat{x}, \\
\vec{p}_2 &= p_b \hat{y} - \frac{m_1}{m_b} p_3 \hat{x}, \\
\vec{p}_3 &= p_3 \hat{x},
\end{aligned}
\tag{26}$$

where  $m_b := m_1 + m_2$ ,  $p_b = m_1 m_2 \sqrt{(1 - e_b)/(m_b r_b)}$  and  $p_3 = m_b m_3 \sqrt{(1 - e_3)/r_3}$ . Notice that we specify the momentum in terms of the eccentricity and the apo-apsis. Therefore, a higher eccentricity given to the external binary implies a stronger perturbation of the inner binary.

The main goal of this study is to characterize the stability and chaos of a hierarchical system as function of the initial apo-apsis  $r_3$ , the eccentricity  $e_3$  of the external binary and the inclination angle  $\iota$  between the os-

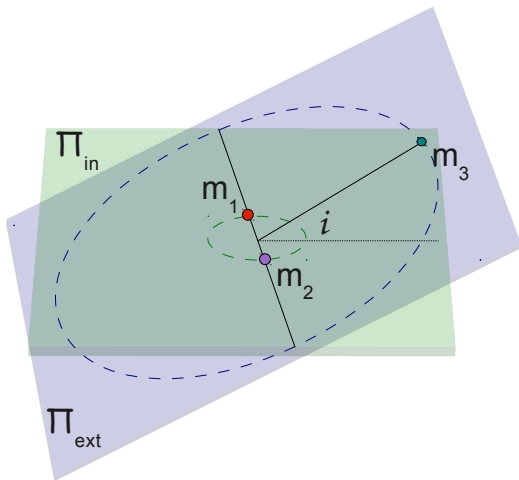


FIG. 4. Hierarchical system (see [39]). Initial configuration of the inner and external binaries. The initial momentum of the third body is given by considering the external binary as a Newtonian binary. Shown are the osculating orbital planes  $\Pi_{\text{in}}$  and  $\Pi_{\text{ext}}$  for inner and external binary orbits. The two planes are inclined by an angle  $\nu$ .

culating orbital planes. We explore the influence of the post-Newtonian corrections.

### 1. Final state survey

An analysis of the asymptotic behavior of the system as function of three parameters  $r_3$ ,  $e_3$  and  $\nu$  was performed. For a given osculating angle  $\nu$ , we produced a map which is a subset of the space of configurations  $(r_3, e_3)$ . We define three possible outcomes which characterize the asymptotic behavior of the system: the escape of one of the bodies, a strong interaction  $H_1^{\%} > 10\%$  and a system which remains stable up to  $t_f = 2 \times 10^7$ . We assign a color for each outcome in a map of initial configurations  $(r_3, e_3)$ , dark gray (color online) for a escape, light gray for a strong interaction and black for a stable configuration. Formally, the result is not a basin boundary map since the outcomes are not attractors in the phase space and the parameters  $(r_3, e_3)$  are not coordinates of the phase space. However, Eqs. (26) gives the link between  $(r_3, e_3)$  and the coordinates of the phase space. On the other hand, a system where one of the bodies escape will be attracted to a hyper-plane in the phase space with one of the spatial coordinates at infinity; a strong interaction may become an escape or the merger of two of the bodies. A merger can be represented by a hyper-plane where two of the bodies share the same values of position and momentum. For a stable system, it is hard to define a single attractor because it can exhibit a different asymptotic behavior for  $t > t_f$ . For simplicity, we refer to our map as basin boundary since it can capture some of the features of a basin boundary.

The choice of  $t_f = 2 \times 10^7$  is motivated by the dy-

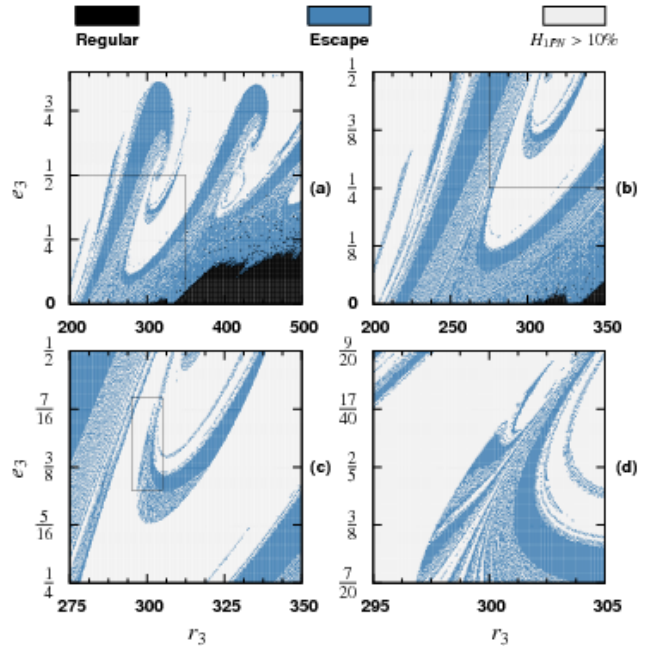


FIG. 5. Fractal basin boundary (Newtonian). Result of the asymptotic behavior of initial conditions for the parameters  $r_3, e_3$  and  $i = 0$  for region  $R_0$  (a),  $R_1$  (b),  $R_2$  (c) and  $R_3$  (d). The black points denotes stable orbits, dark gray points (blue color online) are escapes of the lighter body and light gray points a strong interaction of two of the bodies.

namics of a similar Jacobian system presented in [39]. Including up to 2.5 PN terms, the inner binary arrive to the merger phase after  $t_{\text{mgr}} \approx 2.7 \times 10^7$ . The assumption is that if a conservative system remains stable until that time then the corresponding radiative system will remain stable until the merger of the inner binary. We selected a shorter time (i.e.,  $t_f < t_{\text{mgr}}$ ) due to the computational cost. However, a set of numerical experiment for different values of  $t_f$  suggest that a non-stable orbit is manifest before  $t_f$ .

We explored the parameter space  $r_3, e_3$  using 4 regions defined by

$$\begin{aligned} R_0 &: [200, 500] \times [0, 1], & \Delta r_3 &= 1, & \Delta e_3 &= 0.0025; \\ R_1 &: [200, 350] \times [0, 0.5], & \Delta r_3 &= 0.5, & \Delta e_3 &= 0.00125; \\ R_2 &: [275, 350] \times [0.25, 0.5], & \Delta r_3 &= 0.25, & \Delta e_3 &= 0.000625; \\ R_3 &: [295, 305] \times [0.35, 0.45], & \Delta r_3 &= 0.05, & \Delta e_3 &= 0.00025. \end{aligned}$$

The domain of  $(r_3, e_3)$  are the Cartesian products and the resolution is denoted by  $\Delta r_3, \Delta e_3$ . Each map was done computing  $300 \times 400$  orbits except by region  $R_3$  which contain  $200 \times 400$  orbits. Fig. 5 shows the result for a Newtonian simulation and osculating angle  $i = 0$ . Notice that  $R_3 \subset R_2 \subset R_1 \subset R_0$ , i.e. each  $R_i$  is a magnification of the region  $R_{i-1}$  (in the figure the sub-regions are indicated by rectangles). Fig. 5 shows a characteristic behavior of a fractal sets; every magnification reveals a more complex structure from which it is possible to distinguish some degree of self-similarity. Table I summarize the quantitative results of the basin boundary.

TABLE I. Newtonian orbits. Here  $d_{\text{box}}$  is the box dimension of the basin boundaries presented in Fig. 5, the columns 'Regular', 'Escape' and ' $H_{1\text{PN}} > 10\%$ ' denote the percent of simulation that have the corresponding final state.

Region	$d_{\text{box}}$	Regular	Escape	$H_{1\text{PN}} > 10\%$
$R_0$	$1.76 \pm 0.015$	8.2%	32.4%	59.4%
$R_1$	$1.84 \pm 0.013$	1.0%	41.3%	57.7%
$R_2$	$1.77 \pm 0.015$	0.0%	24.7%	75.3%
$R_3$	$1.74 \pm 0.007$	0.0%	27.2%	72.8%

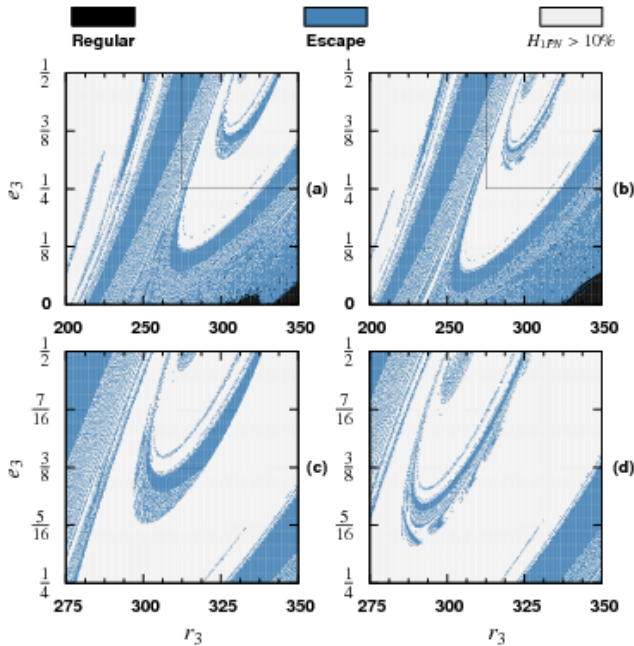


FIG. 6. Fractal basin boundary (Newtonian and 1 PN). Comparison of regions  $R_1$  and  $R_2$  for Newtonian and 1 PN orbits. Panels (a) and (b) show  $R_1$  for Newtonian and 1 PN respectively. Similarly, panels (c) and (d) show  $R_2$  for Newtonian and 1 PN respectively.

Notice that the box dimension reflects the fact that the sets are not perfect self-similar. We choose  $R_1$  and  $R_2$  to perform additional simulations.

A comparison using Newtonian and 1 PN orbits for regions  $R_1$  and  $R_2$  is presented in Fig. 6. There is a clear difference in the set of stable orbits. In the Newtonian case, there are two disjoint sets where the 1 PN system exhibit a single set (compare the black point in panels (a) and (b) of Fig. 6). The magnification  $R_2$  shows differences in the escape and strong interaction sets. The 1 PN case exhibit slightly different substructures (see panels (c) and (d) of Fig. 6). Our comparison includes a set of simulations for leading order spinning 1 PN particles. We employed maximally spinning particles  $\chi_a = 1$  and  $\theta_a = 0, \phi_a = 0$  except by  $\theta_1 = \pi/2, \theta_2 = 2\pi/2$  (see Eq. (4)). Therefore, the initial spin of the particles

(*configuration-a*) is given by

$$\begin{aligned}\vec{s}_1 &= m_1^2 \hat{x}, \\ \vec{s}_2 &= -m_2^2 \hat{x}, \\ \vec{s}_3 &= m_3^2 \hat{z},\end{aligned}\quad (27)$$

Opposite to the non-spinning case, the orbits for our configuration of spinning particles are not coplanar. However, the change in the final states is negligible, the resulting map is almost indistinguishable to the 1 PN case (for brevity we do not display the basin boundaries which are similar to panels (b) and (d) of Fig. 6). The quantitative analysis of the six basin boundaries under comparison is displayed in Table II. The difference on the substructures between the Newtonian case and the 1 PN case are reflected on the box dimension (smaller value for the 1 PN case). In the region  $R_1$ , there is a small change in the distribution of 'Regular', 'Escape' and strong interactions between Newtonian and 1 PN. Nevertheless, in region  $R_2$  there are a noticeable difference in the percentages of 'Escape' and strong interactions. The similarity between the spinning and the non-spinning 1 PN case shows up in the dimension and the distribution of the three outcomes (with minor differences in the percents).

TABLE II. Comparison of Newtonian, 1 PN, radiative 1 PN and leading order spinning 1 PN orbits. Here column PN takes value 0 for Newtonian, 0+1 for 1 PN and 0+1+2.5 for radiative 1 PN. The column Sp takes value 0 for non-spinning particles and 1 for the spinning ones. The meaning of the remaining columns is similar to Table I. See the text for details about the parameters of the spinning case (Fig. 6 and 7 shows the non-spinning cases).

	PN	Sp	$d_{\text{box}}$	Regular	Escape	$H_{1\text{PN}} > 10\%$
$R_1$	0	0	$1.84 \pm 0.013$	1.0%	41.3%	57.7%
	0+1	0	$1.81 \pm 0.014$	1.4%	40.3%	58.3%
	0+1	1	$1.81 \pm 0.014$	1.2%	40.7%	58.1%
	0+1+2.5	0	$1.81 \pm 0.014$	1.7%	40.0%	58.3%
$R_2$	0	0	$1.77 \pm 0.015$	0.0%	24.7%	75.3%
	0+1	0	$1.74 \pm 0.015$	0.0%	18.0%	82.0%
	0+1	1	$1.74 \pm 0.015$	0.0%	18.1%	81.9%

In order of investigate the influence of the gravitational radiation, we performed an evolution which contains the 2.5 PN terms. The inclusion of PN terms is computationally expensive. Therefore, we use a radiative 1 PN Hamiltonian (i.e., we include the Newtonian, 1 PN and 2.5 PN terms in (2)). For similar configurations, the difference in the dynamics between the full 2.5 PN system and the radiative 1 PN is relatively small [39]. Fig. 7 shows the fractal basin boundary and Table II the corresponding quantitative measures. The radiative term does not seem to produce a significant change respect to the inclusion of 1 PN terms (compare Fig. 7 with Fig. 6-(b)). Particularly, the box-dimension of the boundary is the same, and there is only a small difference in the

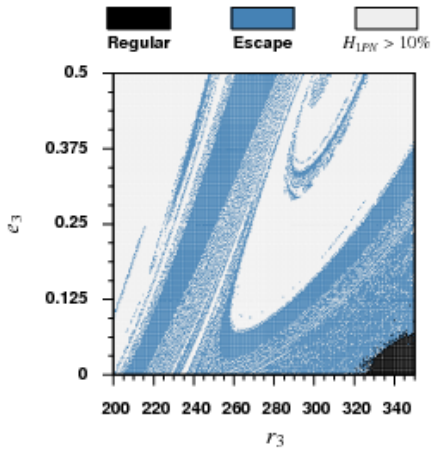


FIG. 7. Basin boundary of region  $R_1$ . The dynamic includes (0+1+2.5) PN terms.

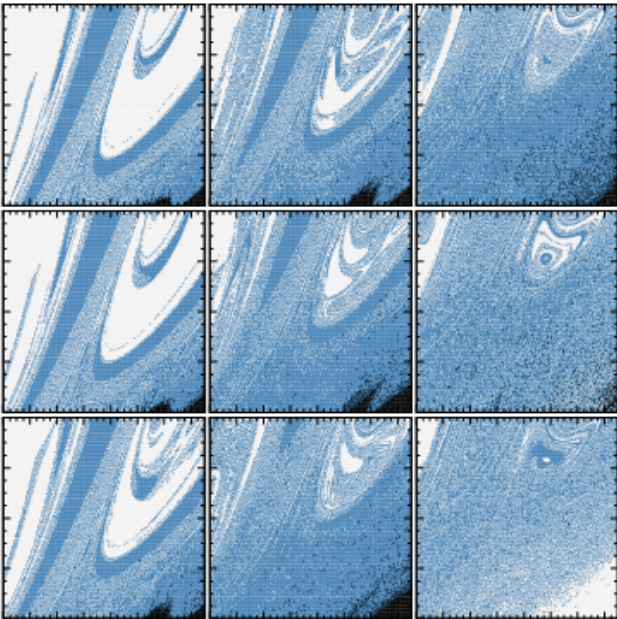


FIG. 8. Fractal basin boundary of region  $R_1$  as function of the osculating angle  $\nu$  (Newtonian). The meaning of the color is the same as in previous plots (see e.g. Fig. 6). From the top to the bottom and from the left to the right  $\nu$  takes the values  $0, \pi/16, \pi/8, 3\pi/16, \pi/4, 5\pi/16, 3\pi/8, 7\pi/16, \pi/2$ .

distribution of the percentages of escapes and strong interactions.

The osculating angle  $\nu$  has a strong influence in the region of the initial parameters  $R_1$ . We produced for the Newtonian case a set of 8 additional maps of region the  $R_1$  for the osculating angle taking the values  $\nu = n\pi/16$ ,  $n \in \{1, 2, \dots, 8\}$ . The result including the case  $\nu = 0$  is presented in Fig. 8. An analogous set of simulations were produced using the 1 PN equation of motion. Fig. 9 show the corresponding basin bound-

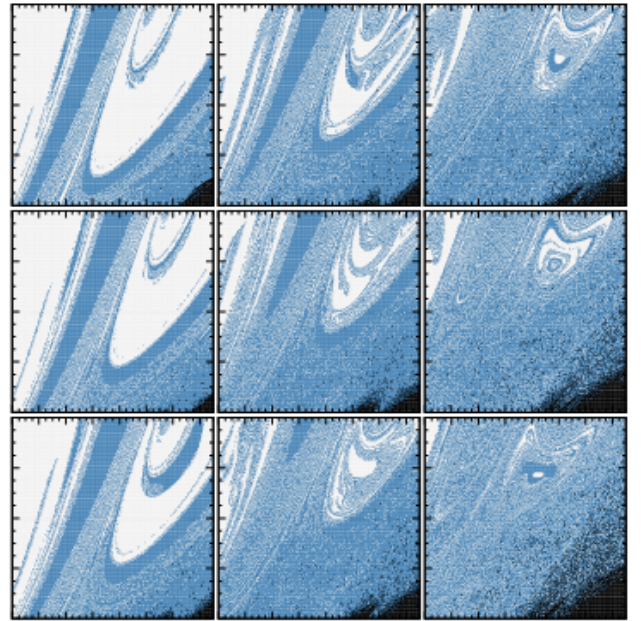


FIG. 9. Fractal basin boundary of region  $R_1$  as function of the osculating angle  $\nu$  (1 PN). The meaning of the color is the same as in previous plots (see e.g. Fig. 6). From the top to the bottom and from the left to the right  $\nu$  takes the values  $0, \pi/16, \pi/8, 3\pi/16, \pi/4, 5\pi/16, 3\pi/8, 7\pi/16, \pi/2$ .

aries. Table III shows the quantitative results for both sets. Notice that for  $i > \pi/4$  the percentage of stable points considerably increase in the 1 PN case respect to the Newtonian. The box dimension in both cases has a growing-oscillatory behavior. Fig. 10 shows the result in terms of the uncertainty exponent  $\alpha$ . A relatively simple function  $\alpha_{\text{fit}}(\nu) = a_i\nu + b_i + c_i \sin \varphi_i\nu$  fits the data. The fit parameters are

$$\begin{aligned}
 a_N &= -0.059 \pm 0.0088, & a_{1\text{PN}} &= -0.097 \pm 0.0065, \\
 b_N &= 0.144 \pm 0.0079, & b_{1\text{PN}} &= 0.183 \pm 0.0059, \\
 c_N &= 0.026 \pm 0.0062, & c_{1\text{PN}} &= 0.018 \pm 0.0047, \\
 \varphi_N &= 7.1 \pm 0.27, & \varphi_{1\text{PN}} &= 6.3 \pm 0.27.
 \end{aligned} \tag{28}$$

The slope of the linear part for the 1 PN is 1.6 times larger than the Newtonian case. However, the oscillatory part is around 0.7 times the 1 PN value with regard to the Newtonian case. This result shows that the chaotic properties of this hierarchical configuration increases in both cases reaching the maximum at  $\nu = \pi/2$ . From the basin boundary figures, the increasing number of unsafe points is noticeable. On the other hand, there is an evident difference for  $\nu = \pi/2$  between the Newtonian and 1 PN basin boundary (compare the bottom-right panel of Figs. 8 and 9). We analyze in detail that particular case in the next section.

TABLE III. Measures of the basin boundaries of Figs. 8 and 9. The osculating angle is denoted by  $\iota$ . The meaning of the remaining columns is similar to Table II.

$\iota$	Newtonian				1 PN			
	$d_{\text{box}}$	Regular	Escape	$H_{1\text{PN}} > 10\%$	$d_{\text{box}}$	Regular	Escape	$H_{1\text{PN}} > 10\%$
0	$1.84 \pm 0.013$	1.0%	41.3%	57.7%	$1.81 \pm 0.014$	1.4%	40.3%	58.3%
$\pi/16$	$1.85 \pm 0.013$	1.0%	43.0%	56.0%	$1.82 \pm 0.014$	0.7%	41.6%	57.7%
$\pi/8$	$1.88 \pm 0.013$	1.1%	49.2%	49.7%	$1.84 \pm 0.013$	0.9%	48.2%	50.9%
$3\pi/16$	$1.92 \pm 0.012$	1.9%	62.3%	35.8%	$1.90 \pm 0.012$	1.5%	58.0%	40.5%
$\pi/4$	$1.91 \pm 0.012$	2.7%	67.9%	29.4%	$1.91 \pm 0.012$	2.2%	64.2%	33.6%
$5\pi/16$	$1.90 \pm 0.012$	2.7%	74.3%	23.0%	$1.91 \pm 0.012$	3.2%	67.9%	28.9%
$3\pi/8$	$1.89 \pm 0.013$	2.2%	77.5%	20.3%	$1.92 \pm 0.012$	4.3%	70.8%	24.9%
$7\pi/16$	$1.94 \pm 0.012$	1.5%	73.9%	24.6%	$1.94 \pm 0.012$	6.1%	69.3%	24.6%
$\pi/2$	$1.98 \pm 0.011$	0.1%	57.1%	42.8%	$1.97 \pm 0.011$	9.3%	67.4%	23.3%

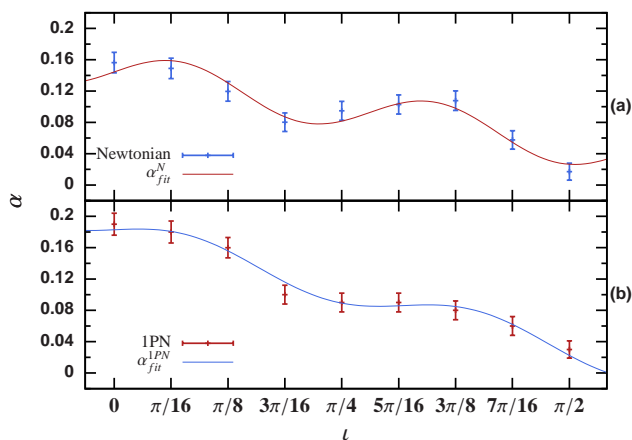


FIG. 10. Uncertainty exponent  $\alpha$  as function of the osculating angle  $\iota$  for the region  $R_1$ . The upper panel (a) shows the result for the Newtonian case, the solid line is the fitting function  $\alpha_{\text{fit}}^{\text{N}}(\iota) = a_{\text{N}}\iota + b_{\text{N}} + c_{\text{N}} \sin \varphi_{\text{N}}\iota$ . The lower panel (b) shows the corresponding result for the 1 PN simulations, where the solid line is  $\alpha_{\text{fit}}^{\text{PN}}(\iota) = a_{\text{PN}}\iota + b_{\text{PN}} + c_{\text{PN}} \sin \varphi_{\text{PN}}\iota$ . The fitting parameters are given in Eq. (28).

## 2. Analysis of orbits

We use the basin boundaries as guide for a detail study of specific orbits. Given the region  $R_1$ , an osculating angle  $\iota$ , two different basin boundaries  $\Omega(r_3, e_3)$  and  $\Omega^*(r_3, e_3)$ , it is possible to produce a new map  $D$  which shows the differences. We constructed the map as follows;  $D(r_3, e_3)$  takes value 1 if  $\Omega(r_3, e_3) = \Omega^*(r_3^*, e_3^*)$  in a neighborhood of  $(r_3, e_3)$  of size at least  $6dr_3 \times 6de_3$ , i.e., for  $r_3^* = r_3 + idr_3$ ,  $e_3^* = e_3 + ide_3$  and  $i \in \{-3, -2, \dots, 3\}$ . If the previous condition is not satisfied, then the  $D(r_3, e_3)$  is set to 0.  $D(r_3, e_3)$  give us a way to identify zones where the two basin boundaries differ in a relatively large region. From the analysis of this map and the basin boundaries, we explore several initial parameters where we compare the orbits for different configurations of the

PN equations of motion. In the following, we describe 5 representative comparisons.

For the region  $R_1$  and  $\iota = \pi/2$  there is a clear difference between the Newtonian and 1 PN evolution (i.e., the difference between the bottom-right panel of Figs. 8 and 9). The bottom-right zone of parameters leads to a different outcome. In the Newtonian case, the simulation with parameters  $e_3 < (r_3 - 310)/320$  ends when  $H_{1\text{PN}} > 10\%$ . However, for the same set of parameters the 1 PN case remains stable. For the Newtonian case, a resonance between the inner and external binaries forces the orbit of the inner binary increasing its eccentricity. However, in the 1 PN case there is no indication of resonance, the orbits remain stable during the simulation (see Fig. 11-(a),(b)). In both cases, the Lyapunov indicator does not show evidence of exponential growth behavior (see Fig. 11-(c)). Additional PN corrections do not change the stability.

For the region  $R_1$  and  $\iota = 0$ , there is a significant difference in the stable orbits between the Newtonian basin boundaries and the 1 PN case (i.e., the black dots in panels (a) and (b) of Fig. 6). Representative orbits which show the difference are presented in Fig. 12. In this case, the coupling between the orbits in the 1 PN case results in the escape of the third body. The Newtonian configuration remains stable without noticeable instability. The Lyapunov indicator shows in the case of 1 PN a characteristic behavior of escape orbits. During a close approach of the three particles, there is a exponential growth of the difference vector followed by a regular behavior which is expected of an uncoupled binary-single body system (see the kink in the Lyapunov indicator of Fig. 12-(c)). The exponential growth in the difference vector is an indication of sensitivity to initial conditions. In general, the resulting escape orbit is chaotic; a small change in the initial condition produces a significant change in the escape direction.

A comparison between 1 PN and 2 PN dynamics shows that similar final outcomes can be the result of different orbits. Many of the studied orbits are almost identical.

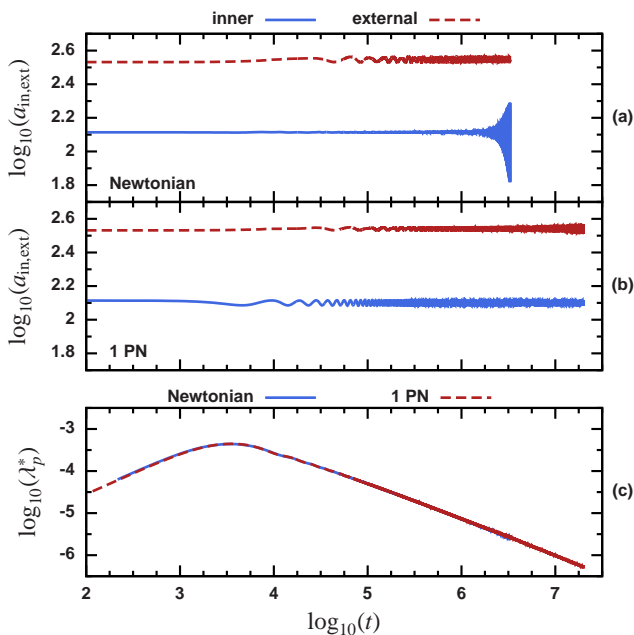


FIG. 11. Semi-major axis and Lyapunov indicator for initial parameters  $\iota = \pi/2, r_3 = 340, e_3 = 0$ . The upper panel (a) shows the semi-major axis  $a$  of the inner and external binaries as function of time for the Newtonian case. The middle panel (b) is similar to (a) but for the 1 PN case. The lower panel (c) shows the Lyapunov indicator for both cases. Notice that the quantities are given in  $\log_{10}$  scales.

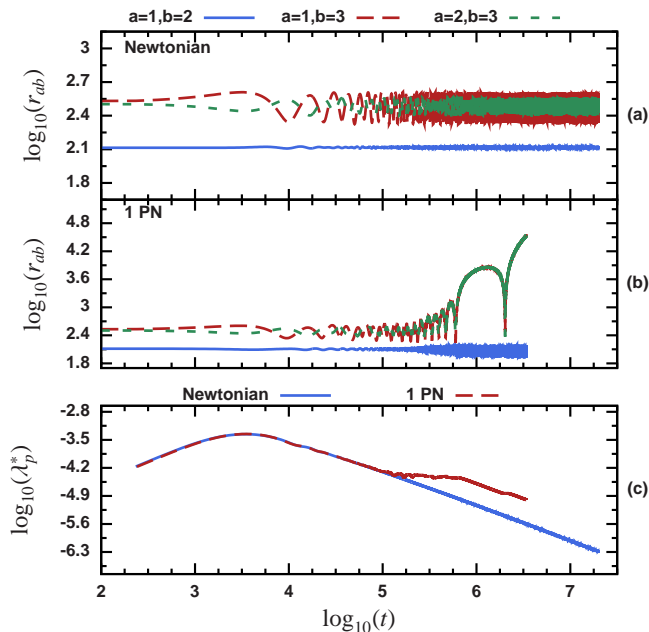


FIG. 12. Relative separation and Lyapunov indicator for initial parameters  $\iota = 0, r_3 = 320, e_3 = 0$ . The upper panel (a) shows the relative separation  $r_{ab}$  between particles as function of time for the Newtonian case. The middle panel (b) is similar to (a) but for the 1 PN case. The lower panel (c) shows the Lyapunov indicator for both cases.

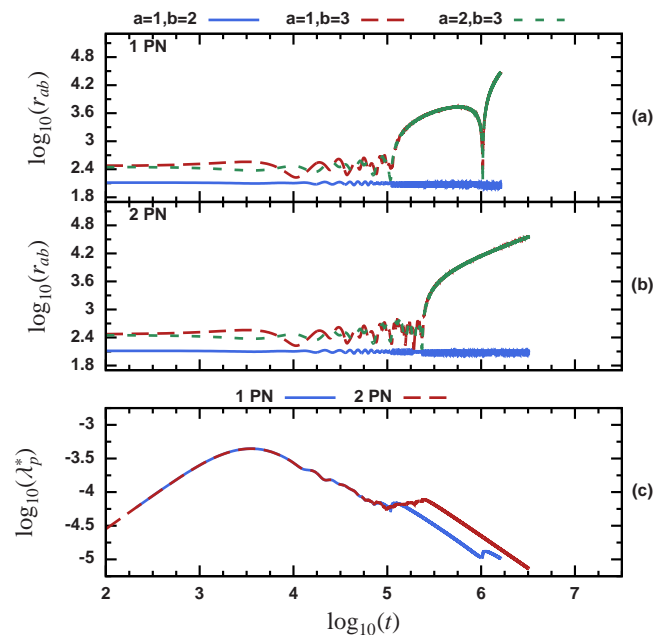


FIG. 13. Relative separation and Lyapunov indicator for initial parameters  $\iota = 0, r_3 = 280, e_3 = 0$ . The upper panel (a) shows the relative separation  $r_{ab}$  between particles as function of time for the 1 PN case. The middle panel (b) is similar to (a) but for the 2 PN case. The lower panel (c) shows the Lyapunov indicator for both cases.

However, there are cases where the evolution is significantly different. Fig. 13 shows the resulted orbits for initial parameters  $\iota = 0, r_3 = 240, e_3 = 0$ . For these initial parameters, the resulting outcome is the escape of the lighter body. Nevertheless, in the 1 PN evolution there is an ejection<sup>1</sup> of the lighter body before the final escape. In contrast, the ejection is not present in the 2 PN orbit (compare panels (a) and (b) of Fig. 13). The Lyapunov indicator shows a significant difference. For the 1 PN case, there is a double kink which correspond to the close encounters before and after the ejection. Nevertheless, the 2 PN evolution presents a single long kink (see Fig. 13-(c)).

For the parameters that we have studied, the inclusion of spin correction has a small influence in the final outcome. However, for some of initial parameters the evolution is completely different. For the initial parameters  $\iota = 0, r_3 = 320$  and  $e_3 = 0.39$ , the 1 PN orbit ends with the strong interaction between particles 1 and 3 (see Fig. 14-(a)). In contrast, the spinning leading order 1 PN for the spin *cifiguration-a* (27) results with the escape of particle 3 (see Fig. 14-(b)). For the escaping orbit, the evolution produces a Lyapunov indicator

<sup>1</sup> In the three-body problem literature, an ejection refers to a temporal large separation of one of the bodies which finally returns [21].

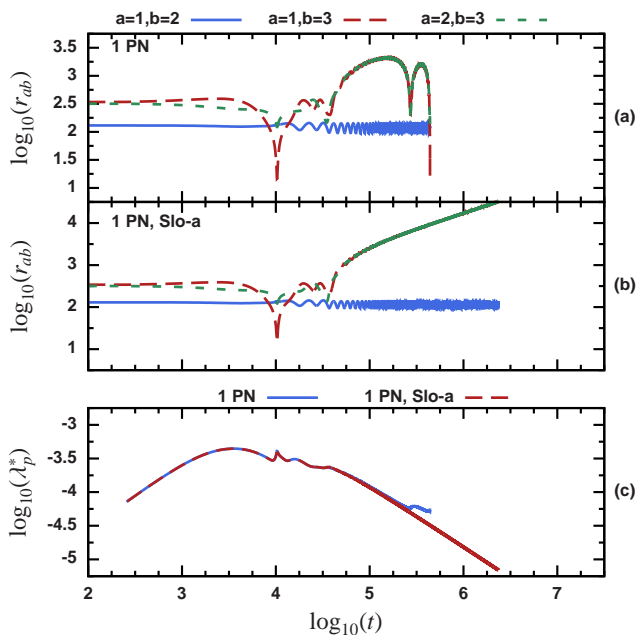


FIG. 14. Relative separation and Lyapunov indicator for initial parameters  $\iota = 0, r_3 = 320, e_3 = 0.39$ . The upper panel (a) shows the relative separation  $r_{ab}$  between particles as function of time for the 1 PN case. The middle panel (b) is similar to (a) but for the leading order spinning 1 PN *configuration-a* (initial spin given by (27)). The lower panel (c) shows the Lyapunov indicator for both cases.

which after  $t = 10^5$  decreases linearly. The Lyapunov indicator shows initially the same structure. However, the strong interaction produces a short kink at the end (see Fig. 14-(c)).

We explored a different set of spin parameters. Here we present one of the results of *configuration-b* given by

$$\begin{aligned} \vec{s}_1 &= m_1^2 \hat{x}, \\ \vec{s}_2 &= m_2^2 \hat{x}, \\ \vec{s}_3 &= m_3^2 \hat{y}. \end{aligned} \quad (29)$$

Fig. 15 shows the result for the initial parameters  $\iota = \pi/4, r_3 = 242, e_3 = 0.2$  for the 1 PN and spinning leading order 1 PN cases. In this evolution, the non-spinning case results in the escape of particle 3. For the spinning particles, the result is the strong interaction between particles 1 and 3. The Lyapunov indicator shows the characteristic exponential growth of the difference vector during the close interaction.

Table IV shows the evolution of the eccentricity of the inner binary  $e_b$ . The eccentricity is computed by calculating numerically the value of the apo-apsis and peri-apsis of the inner binary i.e., computing a sequence of local maxima and minima of  $r_{12}$ . The eccentricity is given by

$$e_b = \frac{r_{\text{ap}} - r_{\text{per}}}{r_{\text{ap}} + r_{\text{per}}}. \quad (30)$$

Notice that the initial value of  $e_b$  in every case is relatively small but not zero due to the perturbation of the third

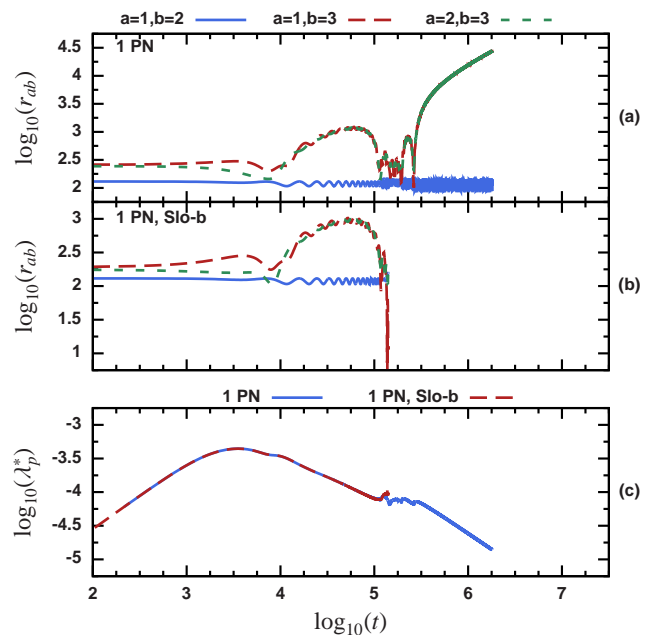


FIG. 15. Relative separation and Lyapunov indicator for initial parameters  $\iota = \pi/4, r_3 = 242, e_3 = 0.2$ . The upper panel (a) shows the relative separation  $r_{ab}$  between particles as function of time for the 1 PN case. The middle panel (b) is similar to (a) but for the spinning leading order 1 PN *configuration-b* (initial spin given by (29)). The lower panel (c) shows the Lyapunov indicator for both cases.

TABLE IV. Evolution of the eccentricity of the inner binary  $e_b$ . Here we refer to the orbits in terms of the figure given in the column 'Fig.',  $e_b(0)$  is the initial eccentricity of the inner binary and  $e_b(t_f)$  the final eccentricity computed before the corresponding simulation finish.  $\langle e_b \rangle$  and  $\sigma(e_b)$  are the arithmetic mean and standard deviation of  $e_b$  respectively. The column 'FS' refers to the final state of the evolution.

#	Fig.	$e_b(0)$	$e_b(t_f)$	$\langle e_b \rangle$	$\sigma(e_b)$	FS
1	11-(a)	0.004	0.493	0.112	0.1453	$H_{1\text{PN}} > 10\%$
2	11-(b)	0.040	0.040	0.039	0.0003	Regular
3	12-(a)	0.021	0.030	0.025	0.0047	Regular
4	12-(b)	0.036	0.281	0.252	0.0556	Escape
5	13-(a)	0.042	0.140	0.117	0.0225	Escape
6	13-(b)	0.062	0.104	0.104	0.0074	Escape
7	14-(a)	0.030	0.155	0.185	0.0332	$H_{1\text{PN}} > 10\%$
8	14-(b)	0.137	0.184	0.184	0.0049	Escape
9	15-(a)	0.095	0.237	0.225	0.0343	Escape
10	15-(b)	0.024	0.004	0.071	0.0299	$H_{1\text{PN}} > 10\%$

body. However, the final value of the eccentricity depends on the final state of the evolution. For regular orbits, the change is relatively small (see the standard deviation of rows 2 and 3 in Table IV). On the other hand, the final eccentricity of the escaping orbits is relatively large during the whole evolution (compare the final eccentric-

ity and the arithmetic mean of the corresponding rows). The case of the orbit with resonance exhibit the larger increment in the eccentricity. The final value before the evolution stop is close to 0.5. For PN evolutions, we did not find evolutions with this kind of resonance. However, a different set of parameters may lead to similar behavior. For a strong interaction with the third body, the resulting final eccentricity is not meaningful since there are two possible outcomes in the full evolution scenario. One possibility is that after the strong interaction the lighter body is ejected or escape leading to a increment in the eccentricity of the inner binary similar to the cases observed. The other possibility is a successive merger of the three bodies.

#### IV. DISCUSSION

We performed a numerical study of stability and chaos of a hierarchical three compact object configuration. The system is composed by a binary system which is perturbed by a third, lighter body initially far away from the binary. For a given inner binary, we explored the influence of the third body taking as free parameters the angle of the osculating orbital planes, the initial apopsis and eccentricity of the third body. Using the basin boundary method, a total of 2,960,000 simulations were analyzed. From the total, 47.3% correspond to Newtonian evolutions, 40.54% to orbits which include (0+1) PN terms, 4.05% to orbits which include (0+1+2.5) PN terms and 8.11% are simulations of spinning particles including leading order in spin and 1 PN terms in the orbital part.

A total of twenty-five basin boundary maps were produced. The basin boundaries exhibit characteristic of fractal sets: some degree of self-similarity and an increasing complexity under magnification. Fractal basin boundaries are an indicator of chaos in dynamical systems. By measuring the fractal dimension of the basin boundaries is possible to determine the uncertainty exponent  $\alpha$ . The property of the exponent is that for  $\alpha \approx 0$  the dynamical system is chaotic and for  $\alpha = 1$  the system is regular. The values of  $\alpha$  for the fractal basin boundaries considered here are between 0.02 and 0.26. The 1 PN set of data produces an exponent slightly larger than the Newtonian case (the maximum difference is 1.6%). On the other hand, the osculating angle  $\iota$  has a strong influence in the uncertainty exponent. The exponent decreases as a linear oscillatory function in the range  $[0, \pi/2]$ . The difference between the planar case ( $\iota = 0$ ) and the case where the third body starts from a direction perpendicular to the orbital plane of the inner binary ( $\iota = \pi/2$ ) is 7.1% for the Newtonian simulations and 8.1% for the 1 PN case.

In Addition to the uncertainty exponent, we quantified the percent of stable orbits, the escapes of the lighter body and strong interactions of two of the bodies. The configurations selected contain between 0% and 9.3% of

stable orbits. The distribution of escapes is between 40.3% and 77.6%. The strong interaction oscillate between 20.3% and 82%. A remarkable case was found at  $\iota = \pi/2$  where the Newtonian simulation present a resonance which drops the number of stable orbits to 0.1%. Opposite to the Newtonian case, a dynamic including 1 PN or higher corrections eliminates the resonance. The number of stable orbits increases to 9.3%. The presence of resonances in the three-body problem is fundamental to understanding the chaotic properties of the system, see e.g. [18, 21, 80] and references therein.

By looking at specific orbits, it is possible to observe some of the different coupling of the inner and external binaries. For most of the orbits, the 1 PN terms have the strongest effect on the dynamics. The inclusion of the spinning particles or 2 PN corrections produces small differences in the orbits which are essentially indential. However, the coupling of the orbits for some of the configurations can produce a significant change in the final outcome. We presented five representative examples.

The spin can produce a significant change in the orbits producing precession of the orbital planes. However, the change on the dynamics is not enough strong to modify the final outcome. On the other hand, gravitational radiation, in general, produces small change in the energy to be significant in the short time scale of the evolution. Similarly to the spinning case, gravitational radiation has a small effect in the asymptotic behavior.

Considering the scenario of a binary system in a galactic core or a region with high density of compact objects, we expect to have the following results. Between a 40% and 70% probability that the lighter body escape the system depending on the relative orbital planes. The remanent binary may result with eccentricities between 0.1 and 0.2. Between 23% and 58% of the bodies may lead to a merger with one of the component of the inner binary; contributing to the growth of the compact objects. The probability of finding a body in a stable orbit is between 1% and 10%, producing a perturbation which lead to small eccentricities of the inner binary of around 0.03. Nevertheless, the combined effect of many bodies of comparable size can significantly change the results.

More general statements about the chaotic behavior of three compact bodies are possible but require an extensive parameter study. Other configurations include for example a characterization of the stability and chaos based on the mass ratios, inner binary separation, magnitude and direction of the spin or initial eccentricity of the inner binary. We consider this a topic for future study.

#### ACKNOWLEDGMENTS

It is a pleasure to thank Todd Oliynyk, Mark Fisher and Bernd Brügmann for valuable discussions and comments on the manuscript. This work was supported in part by ARC grant DP1094582, DFG grant SFB/Transregio 7 and by DLR grant LISA Germany.

- [1] K. Gültekin, M. C. Miller, and D. P. Hamilton, AIP Conf. Proc. **686**, 135 (2003), arXiv:astro-ph/0306204.
- [2] K. Gültekin, M. C. Miller, and D. P. Hamilton, The Astrophysical Journal **616**, 221 (2004), arXiv:astro-ph/0402532.
- [3] K. Gültekin, M. C. Miller, and D. P. Hamilton, The Astrophysical Journal **640**, 156 (2006), arXiv:astro-ph/0509885.
- [4] M. Iwasawa, Y. Funato, and J. Makino, The Astrophysical Journal **651**, 1059 (2006), arXiv:astro-ph/0511391.
- [5] L. Hoffman and A. Loeb, Mon. Not. R. Astron. Soc. **377**, 957 (2007), arXiv:astro-ph/0612517.
- [6] L. Hoffman and A. Loeb, The Astrophysical Journal **638**, L75 (2006), arXiv:astro-ph/0511242.
- [7] A. Gualandris, S. Portegies Zwart, and M. S. Sipior, Mon. Not. R. Astron. Soc. **363**, 223 (Oct. 2005), arXiv:astro-ph/0507365.
- [8] S. Mikkola, Mon. Not. R. Astron. Soc. **203**, 1107 (Jun. 1983), <http://adsabs.harvard.edu/abs/1983MNRAS.203.1107M>.
- [9] S. Mikkola, Mon. Not. R. Astron. Soc. **207**, 115 (Mar. 1984), <http://adsabs.harvard.edu/abs/1984MNRAS.207..115M>.
- [10] M. C. Miller and D. P. Hamilton, The Astrophysical Journal **576**, 894 (2002), arXiv:astro-ph/0202298.
- [11] P. Heinämäki, A&A **371**, 795 (Jun. 2001).
- [12] M. Valtonen and S. Mikkola, Annu. Rev. Astron. Astrophys. **29**, 9 (1991).
- [13] M. Milosavljević and D. Merritt, AIP Conference Proceedings **686**, 201 (2003), <http://link.aip.org/link/?APC/686/201/1>.
- [14] M. J. Valtonen, S. Mikkola, P. Heinämäki, and H. Valtonen, Astrophys. J. Suppl. **95**, 69 (Nov. 1994).
- [15] P. Amaro-Seoane and M. Dewi Freitag, ArXiv e-prints(2010), arXiv:1009.1870 [astro-ph.CO].
- [16] J. Levin and H. Contreras, ArXiv e-prints(Sep. 2010), arXiv:1009.2533 [gr-qc].
- [17] N. Seto and T. Muto, Phys. Rev. D **81**, 103004 (May 2010).
- [18] N. Seto and T. Muto, ArXiv e-prints(2011), arXiv:1105.1845 [astro-ph.CO].
- [19] N. Stone and A. Loeb, ArXiv e-prints(2010), arXiv:1004.4833 [astro-ph.CO]%%CITATION = 1004.4833;%% .
- [20] X. Chen, A. Sesana, P. Madau, and F. K. Liu, Astrophys. J **729**, 13 (2011), <http://stacks.iop.org/0004-637X/729/i=1/a=13>.
- [21] M. J. Valtonen and H. Karttunen, *The three-body problem* (Cambridge University Press, New York, 2006) ISBN 0-521-85224-2 (hardcover).
- [22] J. Levin, Phys. Rev. D **84**, 3515 (Apr. 2000), arXiv:gr-qc/9910040.
- [23] N. J. Cornish and J. Levin, Phys. Rev. D **68**, 024004 (Jul. 2003).
- [24] J. D. Barrow and J. Levin(Mar. 2003), arXiv:nlin/0303070 [nlin.CD].
- [25] J. Levin, Phys. Rev. D **74**, 124027 (Dec. 2006), arXiv:gr-qc/0612003.
- [26] A. Gopakumar and C. Königsdörffer, Phys. Rev. D **72**, 121501 (Dec. 2005), arXiv:gr-qc/0511009.
- [27] W. Han, Gen. Rel. Grav. **40**, 1831 (Sep. 2008), arXiv:1006.2229 [gr-qc].
- [28] J. D. Schnittman and F. A. Rasio, Phys. Rev. Lett **87**, 121101 (Sep. 2001), arXiv:gr-qc/0107082.
- [29] T. Damour, P. Jaranowski, and G. Schäfer, Phys. Rev. D **77**, 064032 (2008), arXiv:0711.1048 [gr-qc].
- [30] J. Steinhoff, S. Hergt, and G. Schäfer, Phys. Rev. D **77**, 081501 (Apr 2008), arXiv:0712.1716 [gr-qc].
- [31] J. Hartung and J. Steinhoff, Phys. Rev. D **83**, 044008 (Feb 2011), arXiv:1011.1179 [gr-qc].
- [32] C. Moore, Phys. Rev. Lett. **70**, 3675 (Jun 1993).
- [33] T. Imai, T. Chiba, and H. Asada, Phys. Rev. Lett. **98**, 201102 (May 2007).
- [34] C. O. Lousto and H. Nakano, Class. Quantum Grav. **25**, 195019 (2008), arXiv:0710.5542 [gr-qc].
- [35] K. Yamada and H. Asada, Phys. Rev. D **82**, 104019 (Nov 2010), arXiv:1010.2284 [gr-qc].
- [36] K. Yamada and H. Asada, ArXiv e-prints(2010), arXiv:1011.2007 [gr-qc].
- [37] T. Ichita, K. Yamada, and H. Asada, ArXiv e-prints(2010), arXiv:1011.3886 [gr-qc].
- [38] J. D. Schnittman, ArXiv e-prints(2010), arXiv:1006.0182 [astro-ph.HE].
- [39] P. Galaviz and B. Brügmann, Phys. Rev. D **83**, 084013 (Apr 2011).
- [40] M. Campanelli, C. O. Lousto, and Y. Zlochower, Phys. Rev. D **77**, 101501(R) (2008), arXiv:0710.0879 [gr-qc].
- [41] C. O. Lousto and Y. Zlochower, Phys. Rev. D **77**, 024034 (2008), arXiv:0711.1165 [gr-qc].
- [42] P. Galaviz, B. Brügmann, and Z. Cao, Phys. Rev. D **82**, 024005 (Jul 2010), arXiv:1004.1353 [gr-qc].
- [43] P. Diener, Class. Quantum Grav. **20**, 4901 (2003), arXiv:gr-qc/0305039.
- [44] G. Jaramillo and C. O. Lousto, ArXiv e-prints(2010), arXiv:1008.2001 [gr-qc].
- [45] M. Ponce, C. Lousto, and Y. Zlochower, ArXiv e-prints(2010), arXiv:1008.2761 [gr-qc].
- [46] T. Szirtes, *Applied Dimensional Analysis and Modeling*, 2nd ed. (Butterworth-Heinemann, 2006).
- [47] L. Blanchet, Living Reviews in Relativity **9** (2006), <http://www.livingreviews.org/lrr-2006-4>.
- [48] M. Maggiore, *Gravitational Waves. Vol. 1: Theory and Experiments* (Oxford University Press, Oxford, 2007) ISBN ISBN-13: 978-0-19-857074-5.
- [49] G. Schäfer, Physics Letters A **123**, 336 (1987).
- [50] T. Damour, P. Jaranowski, and G. Schäfer, Phys. Rev. D **62**, 044024 (2000), gr-qc/9912092.
- [51] T. Damour, P. Jaranowski, and G. Schäfer, Phys. Rev. D **62**, 084011 (2000), gr-qc/0005034.
- [52] T. Damour, P. Jaranowski, and G. Schäfer, Phys. Rev. D **62**, 021501 (2000), erratum-ibid. 63, 029903, (2000), gr-qc/0003051.
- [53] T. Damour, P. Jaranowski, and G. Schäfer, Phys. Lett. B **513**, 147 (2001), gr-qc/0105038.
- [54] J. P. Eckmann and D. Ruelle, Rev. Mod. Phys. **57**, 617 (Jul 1985).
- [55] X. Wu and Y. Xie, Phys. Rev. D **77**, 103012 (May 2008).
- [56] S. W. McDonald, C. Grebogi, E. Ott, and J. A. Yorke, Physica D: Nonlinear Phenomena **17**, 125 (1985), ISSN 0167-2789, <http://www.sciencedirect.com/science/article/B6TVK-46DFBV6-1/2/>

ff15e6e9d5c9db35931760b4e178ba4b.

- [57] J. Farmer, E. Ott, and J. A. Yorke, *Physica D: Non-linear Phenomena* **7**, 153 (1983), ISSN 0167-2789, <http://www.sciencedirect.com/science/article/pii/0167278983901252>.
- [58] H.-O. Peitgen, H. Jürgens, and D. Saupe, *Chaos and Fractals* (Springer, 1993).
- [59] K. Falconer, *Fractal Geometry: Mathematical Foundations and Applications*, 1st ed. (John Wiley & Sons, 1990).
- [60] V. I. Arnold, *Ordinary Differential Equations* (The MIT Press, Cambridge, Ma., 1978) ISBN 0262510189.
- [61] X. Wu and T.-Y. Huang, *Physics Letters A* **313**, 77 (2003), ISSN 0375-9601, <http://www.sciencedirect.com/science/article/pii/S0375960103007205>.
- [62] X. Wu, T.-Y. Huang, and H. Zhang, *Phys. Rev. D* **74**, 083001 (Oct 2006).
- [63] P. Jaranowski and G. Schäfer, *Phys. Rev. D* **55**, 4712 (1997).
- [64] P. Jaranowski and G. Schäfer, *Phys. Rev. D* **57**, 7274 (1998).
- [65] M. Galassi, J. Davies, J. Theiler, B. Gough, G. Jungman, P. Alken, M. Booth, and F. Rossi, *GNU Scientific Library Reference Manual*, 3rd ed. (Network Theory Ltd., 2009) ISBN 0954612078.
- [66] Wolfram Research, Inc., *Mathematica*, version 7.0 ed. (Wolfram Research, Inc., 2008).
- [67] C. A. Burdet, *Zeitschrift Angewandte Mathematik und Physik* **18**, 434 (May 1967).
- [68] D. C. Heggie, *Celestial Mechanics and Dynamical Astronomy* **10**, 217 (Oct. 1974).
- [69] S. Mikkola and S. J. Aarseth, *Celestial Mechanics and Dynamical Astronomy* **47**, 375 (Dec. 1989).
- [70] S. Mikkola and S. J. Aarseth, *Celestial Mechanics and Dynamical Astronomy* **57**, 439 (Nov. 1993).
- [71] S. Mikkola and S. J. Aarseth, *Celestial Mechanics and Dynamical Astronomy* **64**, 197 (Sep. 1996).
- [72] M. Hénon, *Celestial Mechanics and Dynamical Astronomy* **13**, 267 (1976).
- [73] M. Nauenberg, *Physics Letters A* **292**, 93 (Dec. 2001), arXiv:nlm/0112003v2.
- [74] M. D. Hartl and A. Buonanno, *Phys. Rev. D* **71**, 024027 (Jan 2005).
- [75] B. Walther, B. Brügmann, and D. Müller, *Phys. Rev. D* **79**, 124040 (2009), arXiv:arXiv: 0901.0993 [gr-qc] [gr-qc].
- [76] S. Husa, M. Hannam, J. A. González, U. Sperhake, and B. Brügmann, *Phys. Rev. D* **77**, 044037 (2008), arXiv:arXiv:0706.0904v1 [gr-qc] [gr-qc].
- [77] W. Tichy, B. Brügmann, M. Campanelli, and P. Diener, *Phys. Rev. D* **67**, 064008 (2003), gr-qc/0207011.
- [78] E. Berti, S. Iyer, and C. M. Will, *Phys. Rev. D* **74**, 061503 (2006), gr-qc/0607047.
- [79] H. P. Pfeiffer, D. A. Brown, L. E. Kidder, L. Lindblom, G. Lovelace, and M. Scheel, *Class. Quant. Grav.* **24**, S59 (2007), arXiv:gr-qc/0702106.
- [80] R. Mardling, in *The Cambridge N-Body Lectures*, Lecture Notes in Physics, Vol. 760, edited by S. Aarseth, C. Tout, and R. Mardling (Springer Berlin / Heidelberg, 2008) pp. 59–96, 10.1007/978-1-4020-8431-7\_3, [http://dx.doi.org/10.1007/978-1-4020-8431-7\\_3](http://dx.doi.org/10.1007/978-1-4020-8431-7_3).